Clinical and molecular insights into BAFopathies

Sluijs, P.J. van der

Part II

Methods for studying mechanisms of disease and possible treatment

Chapter 7

Developing an *in vitro* model system to study the effects of Coffin-Siris Syndrome pathogenic variants on neuronal differentiation

Pleuntje J van der Sluijs[1], Kelly K D Vonk[2], Serkan Dogan[2], Maja Vukic[2], Lucy J Sinke[2], Christian Freund[3], Bastiaan T Heijmans[4], Gijs W E Santen[1], Lucia Daxinger[2]

Affiliations:
1. Department of Clinical Genetics, Leiden University Medical Center, Leiden, the Netherlands
2. Department of Human Genetics, Leiden University Medical Center, Leiden, the Netherlands
3. LUMC hiPSC Hotel, Dept. Anatomy & Embryology, Leiden University Medical Center, Leiden, The Netherlands.
4. Molecular Epidemiology, Department of Biomedical Data Sciences, Leiden University Medical Center, Leiden, the Netherlands

Manuscript in preparation

ABSTRACT

Coffin-Siris syndrome (CSS) is caused by pathogenic variants in genes encoding the BAF chromatin remodelling -complex. The exact pathophysiological mechanisms underlying CSS are unknown. By using patient derived induced pluripotent stem cells (iPSCs) carrying pathogenic variants in *ARID1B* or *SMARCB1* and differentiation towards neuronal progenitor cells (NPCs), we established an in vitro model system to study variant effects on neuronal differentiation and on the iPSC and NPC epigenetic landscapes. Using RT-qPCR, IF-staining and DNA methylation analyses we show suitability of our cell model for studying CSS variant effects on neuronal differentiation.

INTRODUCTION

Coffin- Siris syndrome (CSS) (OMIM 135900) is characterized by neurodevelopmental delay (NDD), hypotonia, corpus callosum agenesis, distinctive facial features and aplasia or hypoplasia of the fifth digit and/or nails[1]. Pathogenic variants in genes encoding members of the canonical BAF chromatin remodelling complex (SWI/SNF complex), which consists of 15 subunits. Pathogenic variants in seven subunits have been identified as underlying the disease in most CSS patients[2-8]. Pathogenic variants in *ARID1B* are identified in 50-75% of CSS patients[4-6,8].. In addition, 7-12% of CSS patients carry pathogenic variants in *SMARCB1*[4-6,8]. Within the CSS spectrum, *ARID1B* patients generally exhibit a milder phenotype compared to those with pathogenic variants in *SMARCB1*[9]. Like many other developmental disorders[10], CSS patients exhibit a specific DNA methylation pattern in their blood, different from controls and suitable for diagnostics[10].

Understanding the pathophysiology behind the CSS phenotype is crucial for both comprehending the disease and identifying potential treatment targets. From studies performed in mice and human cell models, there are already some indications that specific neuronal processes are affected. For example, in ARID1B haploinsufficient mice[11], fewer inhibitory GABAergic interneurons and increased apoptosis and decreased proliferation were reported. More recently, through the use of an organoid model, it was shown that *ARID1B* haploinsufficient variants reduce chromatin accessibility at specific transcription factor binding sites and downregulate transcriptional programs of the corpus callosum[12]. Furthermore, Pagliaroli *et al.*[13], used an iPSC to neural crest cell differentiation model and found that *ARID1B* is required for exit from pluripotency and that this process is impaired in patient-derived iPSCs. However, despite the publication of several in vivo[11,14-19] and in vitro studies[13,20-23], the exact pathophysiological mechanisms underlying CSS remain enigmatic.

Here, to investigate the pathophysiology of CSS we created a cell model system that focuses on genetic variant effects in neuronal differentiation using two *ARID1B* (mild end of CSS) and three *SMARCB1* (severe end of CSS) patient iPSC lines (Figure 1). This system is designed to explore the molecular aspects of CSS and aims to shed light on how CSS pathogenic variants influence iPSC to neuronal differentiation and the transcriptional and epigenetic processes required for this process.

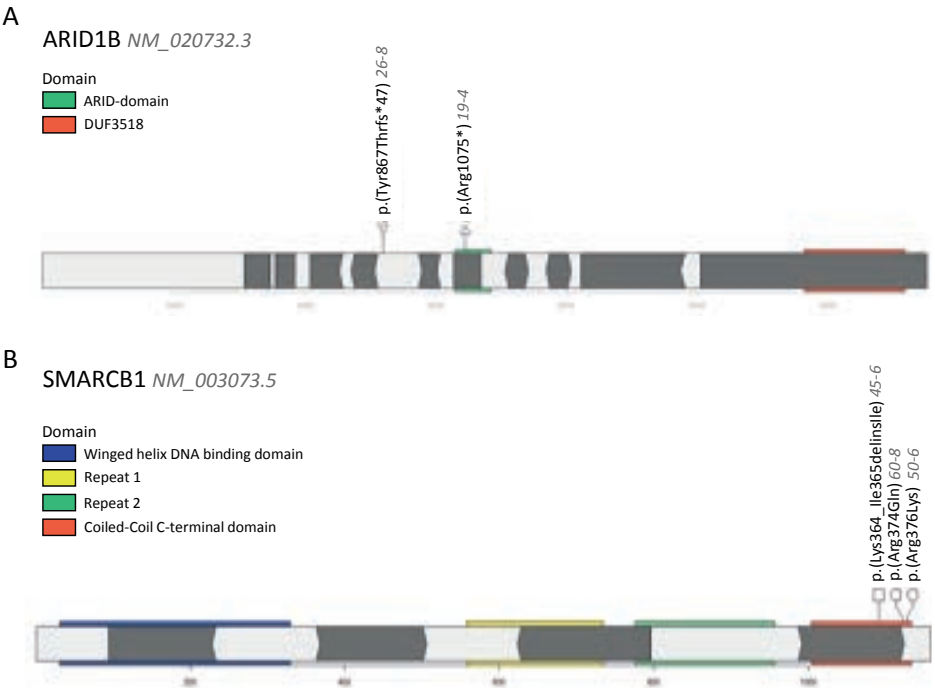

Figure 1: **a**-**b**) Illustration of the *ARID1B* loss of function variants and *SMARCB1* missense variants and inframe deletion of studied patients. The numbers in the gene model refer to transcripts NM_020732.3 (*ARID1B*) and NM_003073.5 (*SMARCB1*).

METHODS

Human iPSC generation and culture

Control iPSC lines (114-1 and 114-2) were derived from fibroblasts obtained from unaffected siblings of spinocerebellar ataxia patients[24]. Line 4-10 was generated from fibroblasts of a healthy 40-year-old control, and line 64-9 was derived from fibroblasts of a mosaic *ARID1A* patient. Skin fibroblasts were obtained from five CSS patients, two patients with a pathogenic variant in *ARID1B*, and three patients with a pathogenic variant in *SMARCB1* (Figure 1a-b). Line 4-10, 64-9, and all patient lines (*ARID1B* patients: 19-4, 26-8; *SMARCB1* patients: 50-6, 45-6, 60-8) were established at the LUMC hiPSC Hotel using the polycistronic lentiviral vector LV.RRL.PPT.SF.hOKSM.idTomato.-preFRT as described elsewhere[25,26].

Informed consent was obtained. The study was conducted in accordance with the criteria set by the Declaration of Helsinki. The protocol to make iPSCs was approved by the institutional review board (IRB) at LUMC.

For each line multiple clones were generated. Their pluripotency was assessed through immunofluorescence microscopy using antibodies against NANOG, OCT3/4, SSEA4, and Tra-1-81. After spontaneous differentiation into three germ layers antibodies against TUBB3, AFP and CD31 were used, as described by Warlich *et al*[26]. Clones exhibiting pluripotent characteristics were selected for downstream applications. Karyotyping by G binding was performed, and short tandem repeat (STR) profiling was carried out. Expansion of iPSC lines occurred in feeder-free, serum-free mTeSR™1 medium (STEMCELL Technologies), with passaging performed at a ratio of approximately 1:10 at 80% confluency using ReLeSR (STEMCELL Technologies). Small cell clusters (50–200 cells) were then plated on tissue culture dishes coated overnight with Corning® Matrigel® matrix (Corning) or Geltrex™ LDEV-Free hESC-qualified Reduced Growth Factor Basement Membrane Matrix (Fisher-Scientific).

Differentiation into medial ganglionic eminence (MGE) progenitors/neuronal progenitor cells (NPC)

iPSC lines were differentiated towards medial ganglionic eminence progenitors (MGE) or NPCs using an adaption of the protocol to produce GABAergic interneurons by Liu *et al*[27] (Figure 2). In brief, iPSCs were dissociated with accutase and suspended in STEMdiff neural induction medium (NIM), supplemented with SMADi and Y-27632. iPSCs were transferred to an AggreWell800 plate (all STEMCELL Technologies, Vancouver, Canada), with daily refreshing of NIM. After 7 days, embryoid bodies were moved to a poly-D-lysine (PDL)/laminin-coated 6-well plate. NIM was changed every other day until day 10, when neural rosettes appear. On day 10, 1.5 µM Pur was added to the medium, with refreshing of NIM+Pur every other day until day 16. On day 16, the differentiating colonies contain neural tube–like rosettes formed by multiple layers of columnar epithelia surrounded by a ring of flat cells.

Differentiation was performed twice. On day 12 DNA and RNA was harvested and cells were fixed for immunohistochemistry. During the second differentiation, neural tube-like rosettes were harvested on day 16 for DNA and RNA.

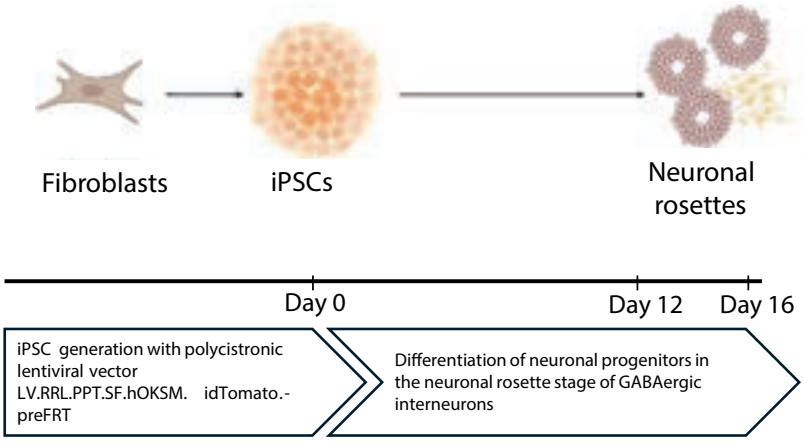

Figure 2: Schematic representation Neural differentiation of patient-derived induced pluripotent stem cells (iPSCs) to neural progenitor cells

Immunofluorenscence (IF)

Cells were fixed with 4% paraformaldehyde (PFA) for 30 min at room temperature. Cells were pre-incubated for 10 minutes at room temperature in 0.1-1.0% Triton X-100 in Dulbecco's phosphate-buffered saline (dPBS) and subsequently blocked for 30 minutes with 1% bovine serum albimun (BSA) in dPBS. Primary antibodies were diluted in 1% BSA in dPBS and samples were incubated in a humidified chamber overnight at 4°C. Secondary antibodies were diluted in 1%BSA in dPBS and samples were incubated for 2 hours at room temperature. Finally, samples were covered with Everbrite hardset containing 4', 6-diamidino-2-phenylindole (DAPI) (Biotum, USA). Antibodies are reported in Supplementary Table 1.

Real-time quantitative polymerase chain reaction (RT-qPCR)

Total RNA was isolated using QIAzol (5346994; Qiagen), with approximately 1 mg of total RNA utilized for reverse transcription via the RevertAid H Minus First Strand cDNA Synthesis Kit (K1632; Thermo). RT-qPCR was performed in triplicate on a C1000TM Thermal cycler (Bio-Rad) with SYBR Green (170-8887; Bio-Rad). Expression data were normalized to GUS. Primer sequences are reported in Supplementary Table 2.

DNA methylation analyses

Omixer[28] was used to randomize DNA samples to optimize sample distribution across batches. Raw DNA methylation data was obtained from Illumina HumanMethylationEPIC arrays (array type: EPICv2). The analyses were conducted in R version 4.3.2 using the following R packages: ChAMP, RPMM, Minfi, ggplot2, DNAmArray, irlba, pheatmap, wateRmelon, ggfortify, shinyMethyl, IlluminaHumanMethylation450kanno.ilmn12.hg19,

GenomicRanges package, ComplexHeatmap, and limma. Data processing and analysis were performed using Python version 3.8.5, and the following Python libraries: Pandas (version 1.2.4), NumPy (version 1.19.5), Scikit-learn (version 0.24.2), Matplotlib (version 3.4.3) and Seaborn (version 0.11.2).

RESULTS

Characterization of *ARID1B* and *SMARCB1* patient-derived iPSC lines

To create an *in vitro* model system focusing on variant effects in neuronal differentiation in CSS we generated iPSC lines from fibroblasts of two patients with pathogenic variants in *ARID1B*, three patients with pathogenic variants in *SMARCB1* (Figure 1a-b) and four control iPSC lines. All iPSC lines expressed the pluripotency marker genes *OCT4* and *NANOG* and there was no statistical significance in mRNA levels between controls and patients when measured by RT-qPCR (Figure 3a-b). Furthermore, control and patient-derived iPSCs showed a similar morphology. In accordance with the RT-qPCR data, immunofluorescence (IF)-staining showed expression of the pluripotency marker OCT4 (Figure 3c).

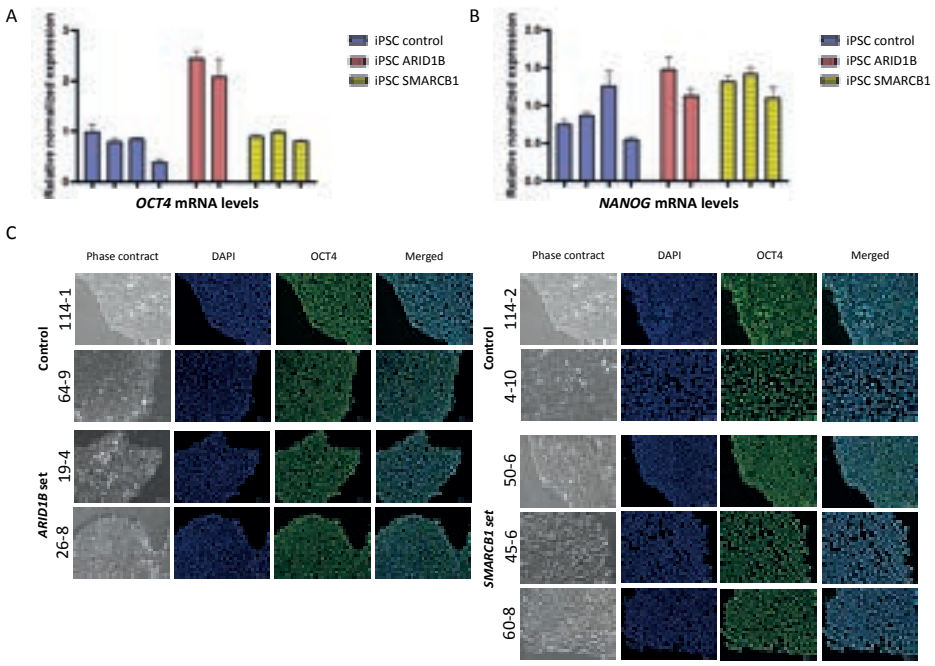

Figure 3: **a**-**b**) mRNA levels of *OCT4* and *NANOG*. **c**) IF-staining of OCT4 and DAPI.

Since increased apoptosis of neuronal progenitors was observed in ARID1B haploinsufficient mice[11,29], we investigated whether increased apoptosis is present in patient-derived iPSC using IF-staining of cleaved caspase-3. We found a similar cleaved caspase-3 staining in patient and control lines (Figure 4), suggesting that neither *ARID1B* nor *SMARCB1* CSS pathogenic variants lead to increased apoptosis of iPSCs.

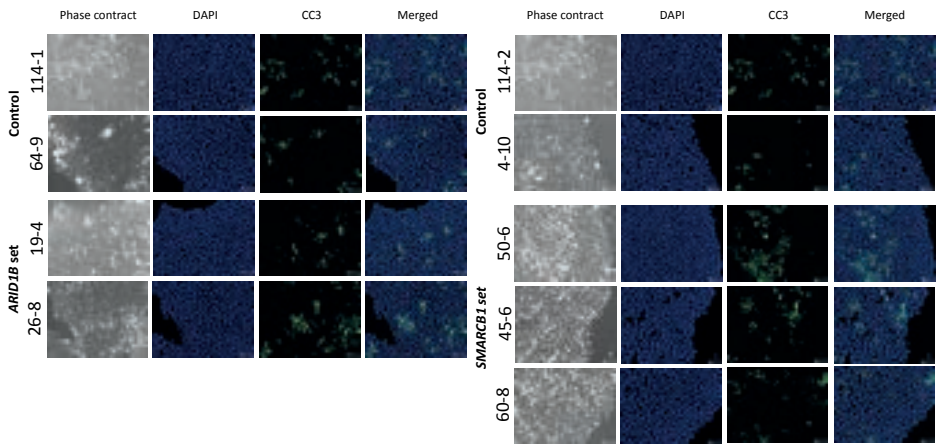

Figure 4: IF-staining of cleaved caspase-3 (CC3) and DAPI in iPSCs.

Next, we addressed the effect of the *ARID1B* and *SMARCB1* pathogenic variants on mRNA levels. The two *ARID1B* patient lines both have pathogenic variants that lead to premature stop codons (Figure 1a), and *ARID1B* haploinsufficiency[13]. Using RT-qPCR, we found that *ARID1B* mRNA levels in the *ARID1B* patient lines were slightly reduced, but not statistically significantly lower, when compared to control or *SMARCB1* patient lines (Figure 5a), most likely due to incomplete nonsense-mediated decay. The three *SMARCB1* pathogenic variants are all nontruncating variants (i.e. missense variants or in frame deletions) (Figure 1b). Consistent with this, *SMARCB1* mRNA levels were similar in *SMARCB1* patient when compared to control lines by RT-qPCR (Figure 5b). Together, these results show that iPSCs derived from patients with a pathogenic variant in either *ARID1B* or *SMARCB1* are pluripotent and phenotypically similar to iPSCs derived from healthy controls.

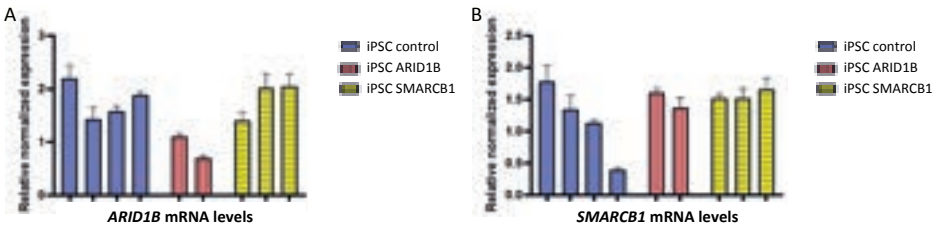

Figure 5: **a**-**b**) mRNA levels of *ARID1B* and *SMARCB1* in iPSCs.

A cellular model system to study CSS variant effects on neuronal differentiation

Next, we differentiated control and patient iPSC lines towards early neuronal progenitor cells (NPCs) and subsequently to neuronal rosettes, using an adapted protocol previously published by Liu *et al*[27] (Figure 2). Differentiation was performed twice.

In the first experiment, iPSCs were differentiated for 12 days towards NPCs. This is an intermediary timepoint, which was included to evaluate the differentiation process and to measure apoptosis levels in the various cell lines. The two *ARID1B* and three *SMARCB1* patient lines were differentiated separately, each set together with two control cell lines. Visual inspection of NPCs on day 12 revealed no obvious differences in cell morphology between control and CSS cell lines. We then measured mRNA levels of neuronal progenitor (*NESTIN*, *PAX6* and *SOX2*) and pluripotency marker (*OCT4*) genes by RT-qPCR. These data revealed no statistically significant differences in neuronal progenitor marker gene expression between patient and control NPCs (Figure 6-a-b), despite some variation between the individual cell lines. Furthermore, *OCT4* mRNA expression was only detected in an iPSC control but not in any of the NPC lines (Supplementary Figure 1a). This was verified by IF-staining of OCT4 in NPCs (Supplementary Figure 1b). In addition, we performed IF-staining for the neuronal markers SOX1 and MAP2 and observed similar signals in control and patient NPCs (Figure 6c-d). Finally, IF staining also showed no obvious differences in signal for the apoptosis marker cleaved caspase-3 between control and patient NPC lines (Figure 7). Altogether, these results suggest that *ARID1B* and *SMARCB1* patient-derived iPSCs can be differentiated to day 12 NPCs without showing increased levels of apoptosis.

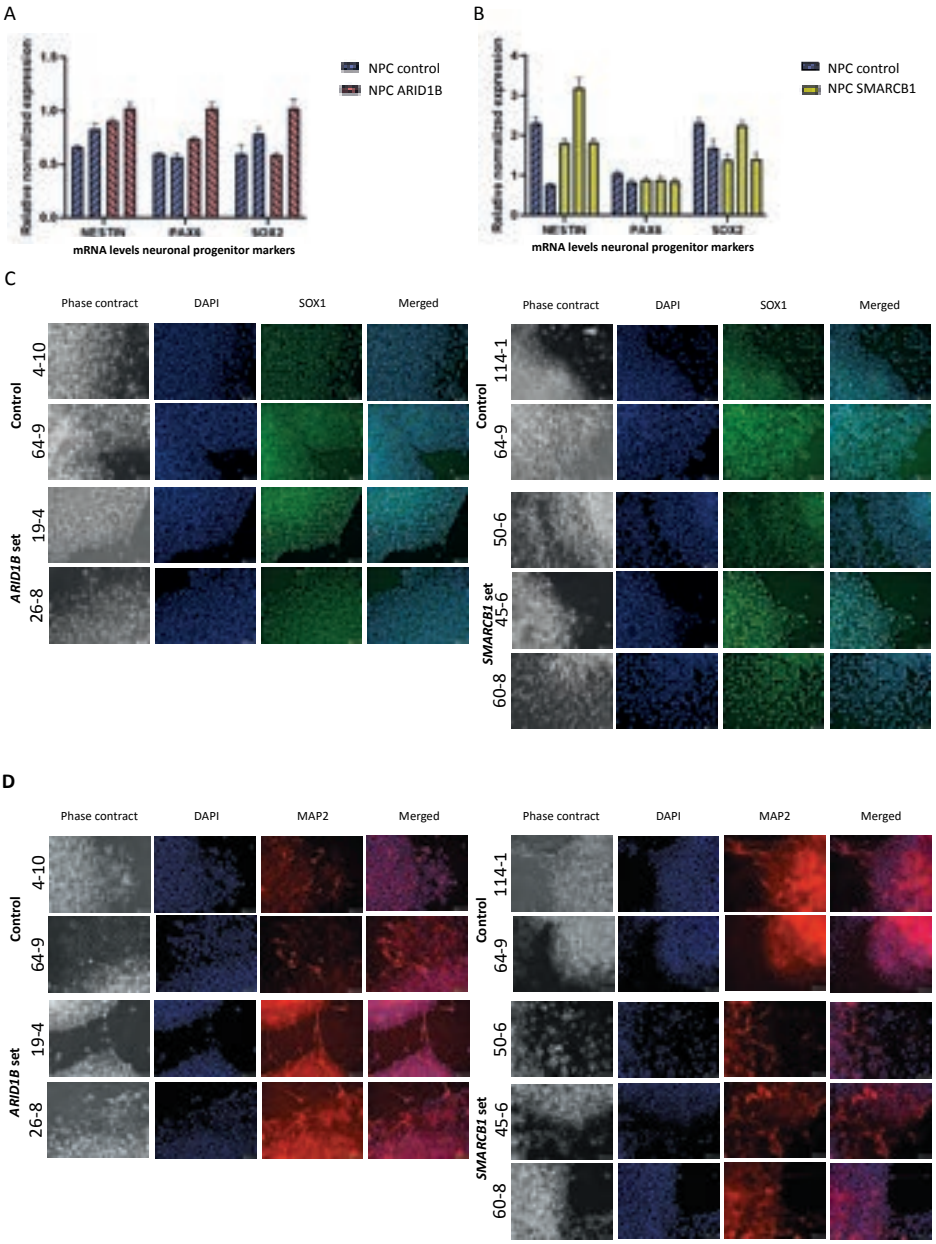

Figure 6: **a**-**b**) mRNA levels of *NESTIN*, *PAX6* and *SOX2* in day 12 differentiated cells. **c**-**d**) IF-staining of SOX1 and MAP2 on day 12 differentiated cells.

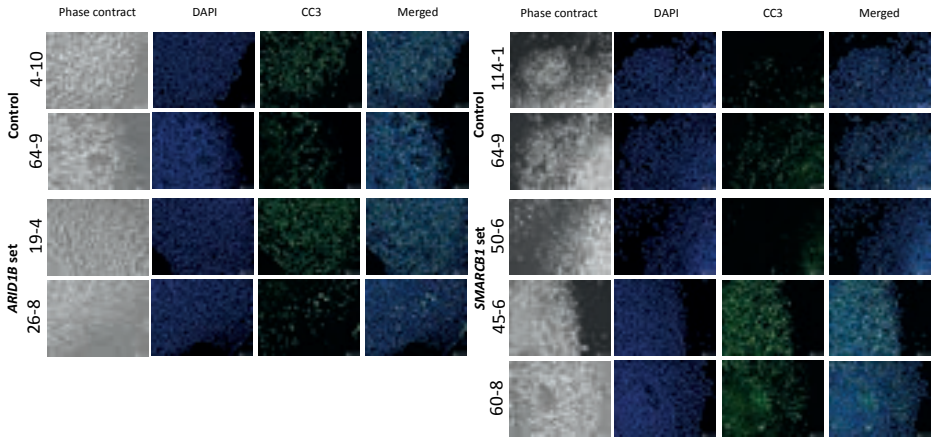

Figure 7: IF-staining of cleaved caspase-3 (CC3) in day 12 differentiated cells.

Next, we differentiated control and patient iPSC lines until day 16, when neuronal rosette formation can be observed[27]. Visual inspection at day 16 revealed that when compared to controls, neuronal rosettes of *ARID1B* patients appeared smaller while *SMARCB1* patient neuronal rosettes showed no obvious morphological differences (Figure 8a). When measured by RT-qPCR, we found that mRNA levels of neuronal (progenitor) markers (*NESTIN*, *PAX6*, *SOX2*, *MAP2*) did not differ significantly between control and *ARID1B* patient neuronal rosettes (Figure 8b). Performing these experiments in *SMARCB1* cell lines revealed largely similar results except for a small, yet statistically significant, reduction in *PAX6* mRNA levels (Figure 8c). We did not detect *OCT4* mRNA expression in *ARID1B* and *SMARCB1* patient neuronal rosettes (Supplementary Figure 2). This result is in agreement with our observations after 12 days of differentiation (Supplementary Figure 1a-b), and suggests that in our model system *ARID1B* haploinsufficiency does not impair exit from pluripotency. Combined, these results indicate that both *ARID1B* and *SMARCB1* patient-derived iPSCs can be successfully differentiated to day 12 neuronal progenitor cell populations and that day 16 neuronal rosettes express neuronal marker genes at levels largely similar to controls.

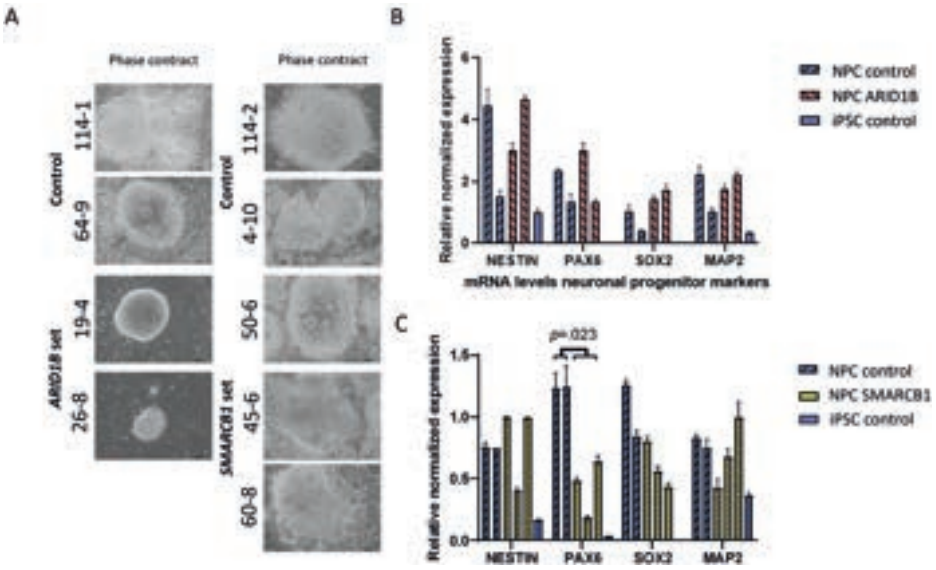

Figure 8: **a**) Phase contrast microscopy images taken at differentiation day 16 of control and patient lines, showing relatively small neuronal rosettes in *ARID1B* patient lines, and in *SMARCB1* patient lines neuronal rosette appear larger compared to control lines. **b**-**c**) mRNA levels of neuronal progenitor markers: *NESTIN*, *PAX6*, *SOX2*, *MAP2* in day 16 differentiated cells.

Genome-wide DNA methylation analysis in control and CSS patient-derived iPSCs and NPCs

Previous studies have reported DNA methylation differences between *ARID1B* and *SMARCB1* patient samples and controls in blood[10], which can be used for CSS diagnostics. However, it is currently not known whether these CSS-associated methylation differences, termed BAFopathy episignatures, are also present in tissue and cell types other than blood. Therefore, we next asked whether the blood-BAFopathy episignature can also be detected in iPSCs and/or NPCs. While iPSCs represent the earliest stage where we may observe differences in DNA methylation levels between patient and control cell lines, NPCs represent a BAFopathy phenotype relevant cell type.

For the genome-wide DNA methylation profiling, we used the Illumina 900K bead chip array that enabled us to measure methylation levels of ~900K CpGs genome-wide in control and patient-derived iPSCs and NPCs (Figure 9a). After quality control and filtering, 889.162 probes were retained per sample for further analysis. We observed that control iPSCs had median b-values ranging between 0.697 and 0.772, while *ARID1B* patient-derived iPSCs showed median b-values between 0.709 and 0.712. For *SMARCB1* patient-derived iPSCs, we measured median b-values between 0.746 and 0.788 (Figure 9b, Supplementary Table 3). For the NPCs, median b-values were ranging

A

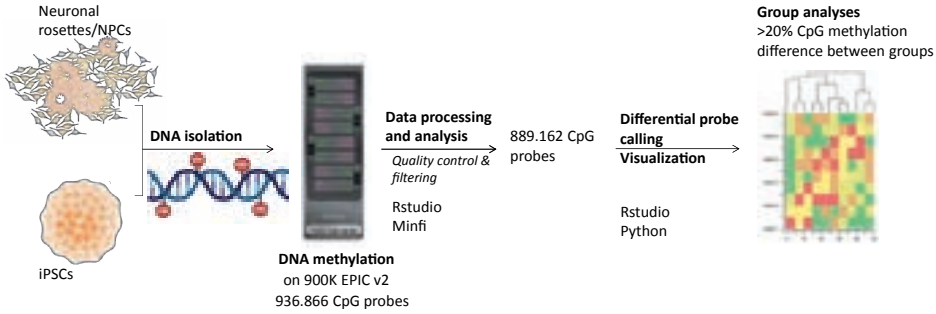
Neuronal rosettes/NPCs
iPSCs
DNA isolation
DNA methylation
on 900K EPIC v2
936.866 CpG probes
Data processing and analysis
Quality control & filtering
Rstudio
Minfi
889.162 CpG probes
Differential probe calling
Visualization
Rstudio
Python
Group analyses
>20% CpG methylation difference between groups

B

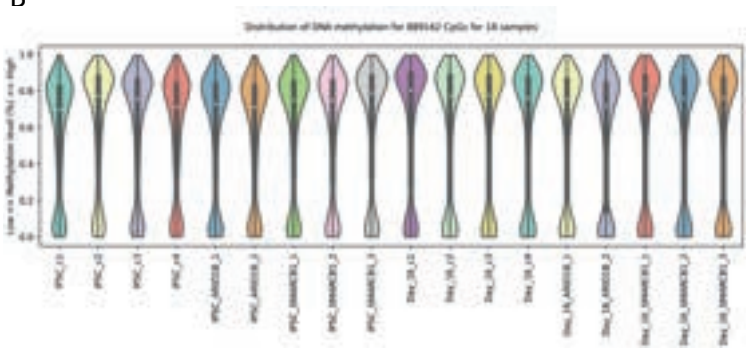

C

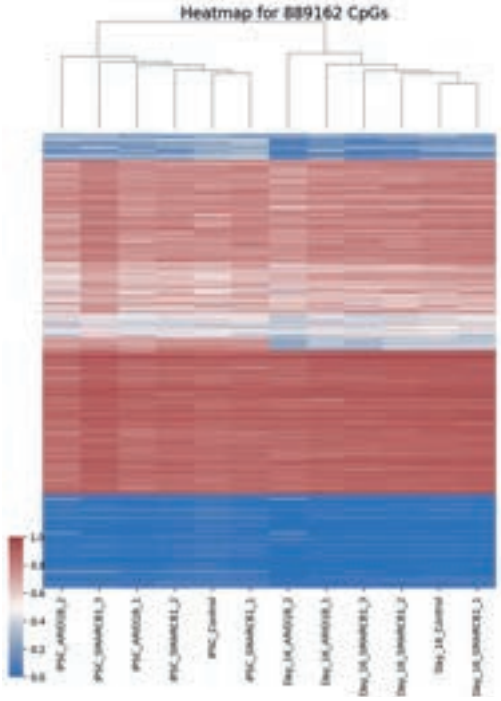
Heatmap for 889162 CpGs

7

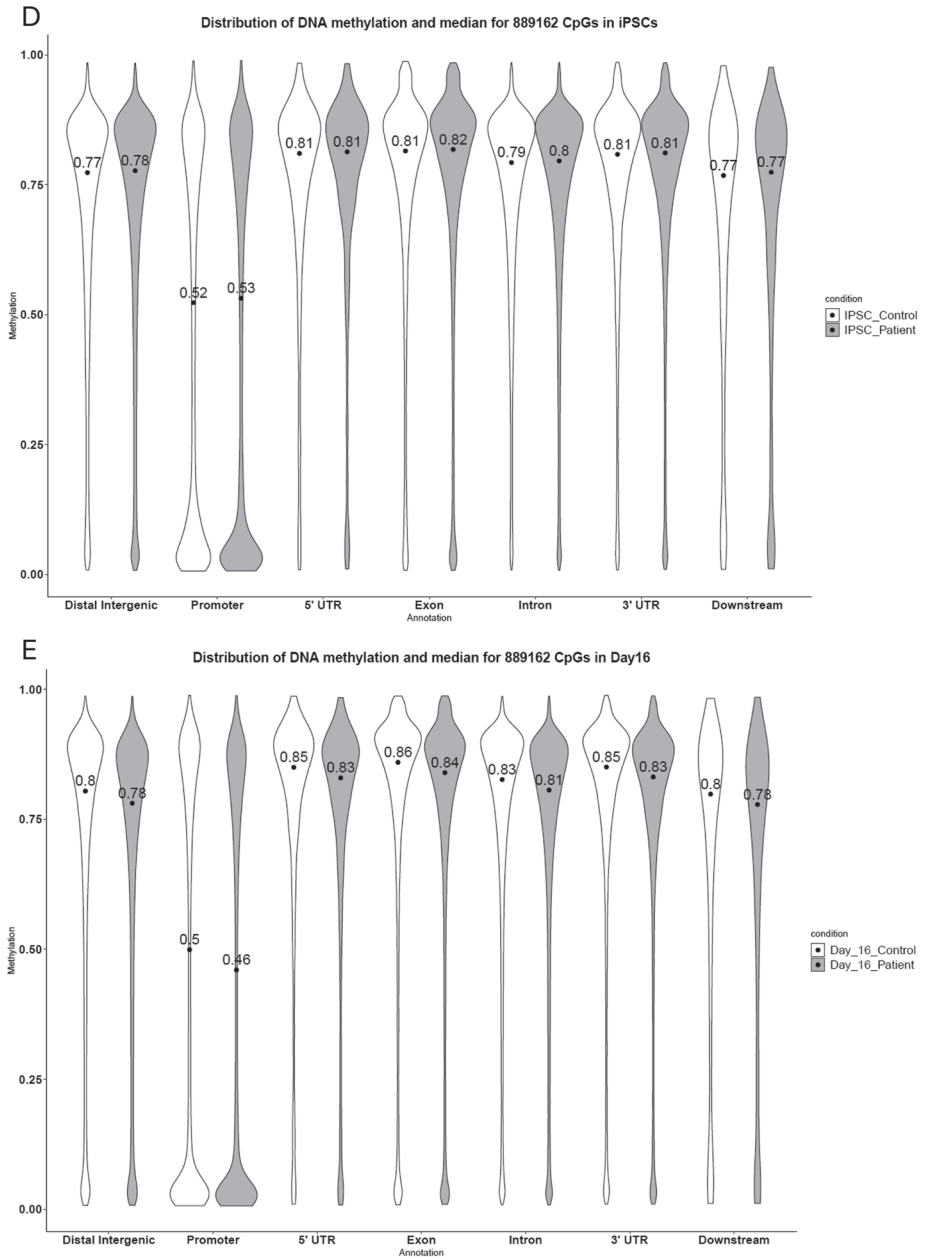

Figure 9: DNA methylation in iPSC and differentiation day 16. **a**) Representation of DNA methylation analysis. 900K EPIC v2 picture derived from https://emea.illumina.com/. **b**) Violin plots depicting individual samples' DNA methylation Beta values, white dots represent median values and black lines kernel density estimates. **c**) Heatmap showing DNA methylation for all 889162 CpGs in iPSC and NPC samples. Rows represent the CpG probes, and columns represent the samples. The color scale from dark blue to dark red represents the range of the methylation levels (beta values) between 0 and 1. **d**) Violin plots depicting DNA methylation Beta values of genomic regions of iPSCs per sample type. **e**) Violin plots depicting DNA methylation Beta values of genomic regions of NPCs per sample type.

between 0.761 and 0.801 for the controls, between 0.717 and 0.754 for the *ARID1B* samples and between 0.758 and 0.779 for the *SMARCB1* patient-derived NPCs (Figure 9b, Supplementary Table 3). Overall, this suggests that *ARID1B* haploinsufficiency and *SMARCB1* disruption, do not alter global DNA methylation levels in iPSCs and NPCs. Importantly, iPSCs clustered differently from NPCs (Figure 9c), which is expected because DNA methylation patterns are cell type-specific.

We next assessed DNA methylation levels for different genomic annotations including genic (promoters, exons, 5'and 3' UTRs, introns) and intergenic (distal intergenic downstream) regions. We found that in iPSCs, median b-values were similar between control and patient samples (Figure 9d). For the NPCs, we observed slightly lower (delta ~0.02%) median b-values in the patient when compared to the control samples for all genomic regions (Figure 9e).

Then, we asked whether the known blood BAFopathy episignature can be detected in iPSCs and/or NPCs. Therefore, we applied the described[10] BAFopathy probes to the iPSC and NPC control and CSS-patient samples. By using this set of CpGs (*n*=121), we found that the iPSC samples formed a cluster that is different from the NPCs (Figure 10a-b). However, within one cell type, patient and control samples clustered together and we could not find any evidence that the blood BAFopathy episignature is present in *ARID1B* or *SMARCB1* patient-derived iPSCs or NPCs. This suggests the BAFopathy pattern from blood is either generated further in the differentiation process or that the observed episignature in blood is tissue specific.

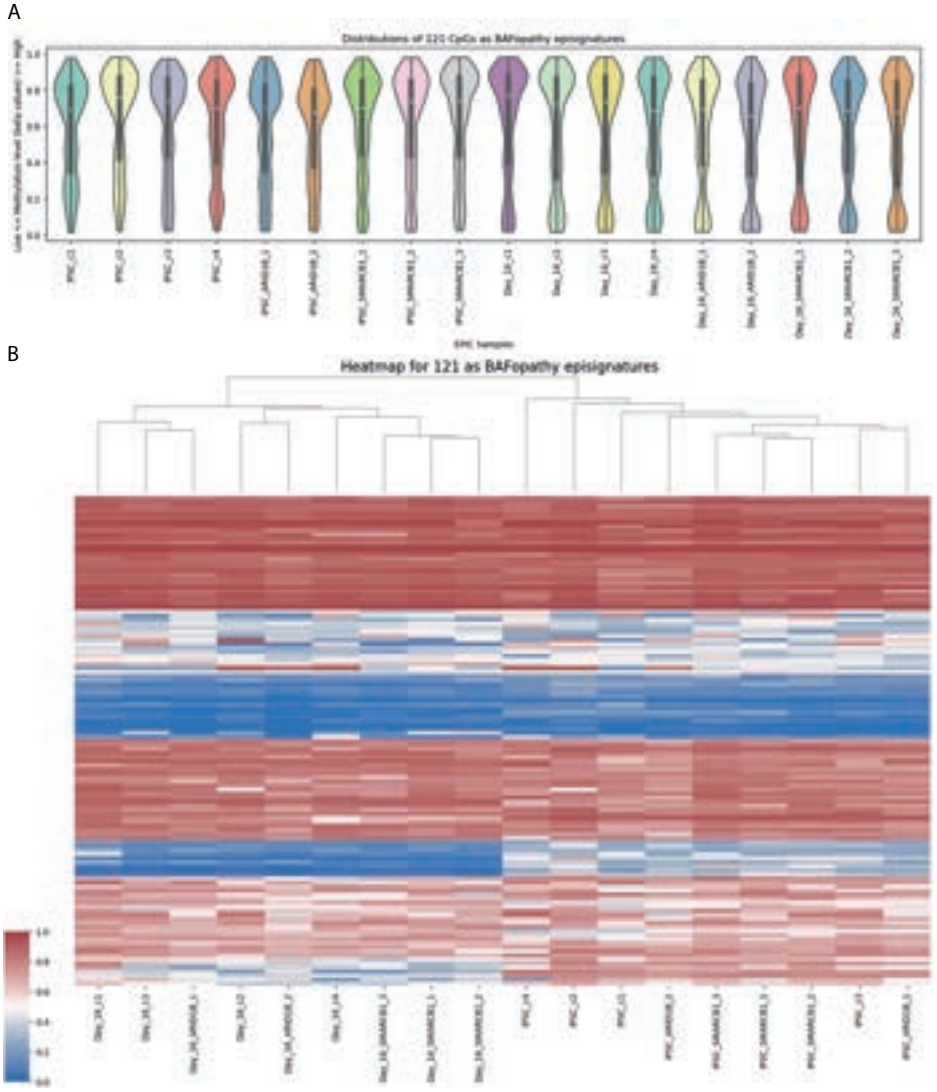

Figure 10: DNA methylation in iPSC and differentiation day 16. (**a**) Distribution of beta-values of the BAFopathy episignature probes per sample. (**b**) Clustering analysis using the BAFopathy episignature probes of iPSC control and NPC day 16 control samples. Rows represent the CpG probes, and columns represent the samples. The color scale from dark blue to dark red represents the range of the methylation levels (beta values) between 0 and 1.

DISCUSSION

Pathogenic variants in genes encoding subunits of the BAF-complex, including *ARID1B* and *SMARCB1*, lead to varying degrees of NDD in CSS patients. Understanding how these variants impact brain development remains challenging due to the difficulty of obtaining human brain samples, and findings from animal studies may not always translate to humans. Here, we employed an *in vitro* model that enables the study of neuronal differentiation differences between patients and controls, as well as within patient groups. The latter is of interest because CSS patients show a spectrum of disease severity that is linked to the underlying genetic defect, suggesting that there could be differences in cellular responses between CSS pathogenic variants.

In iPSCs, we did not observe any overt morphological differences between control and patient cell lines and when measuring expression of pluripotency markers. Furthermore, we showed that in both *ARID1B* and *SMARCB1* patient NPCs, expression of pluripotency markers was silenced, suggesting a successful exit from pluripotency. This differs from a previous observation by Pagliaroli *et al*[13], where they reported an inability of *ARID1B* patient-derived iPSCs to exit pluripotency using a 14-day differentiation paradigm towards neural crest cells. Therefore, it appears that the *ARID1B*-associated impaired exit from pluripotency is not detectable in all neuronal differentiation processes. In line with such a hypothesis, no defects in the exit from pluripotency in *ARID1B* patient-derived iPSCs were reported in a corpus callosum organoid model[12]. Combined, these observations suggest that the effects of CSS variants could be cell type-specific. Indeed, it has previously been reported that ARID1B can take on cell-type-specific roles in transcriptional regulation, where it can function in transcription activation in some cells[30] and transcriptional repression in other cell types[31].

Upon differentiation towards the neuronal lineage, we did observe morphological differences between patient and control cell lines. More specifically, on differentiation day 16, *ARID1B* patient lines exhibited smaller neuronal rosettes, while rosettes from *SMARCB1* patient lines appeared larger than those from control lines. This is interesting since CSS patients with *SMARCB1* mutations show a more severe phenotype. Although preliminary, our findings indicate that additional work will be required to characterize the observed morphological differences and the underlying molecular alterations in detail and it will be important to determine any influences on neuronal function. For instance, differentiation to mature GABAergic interneurons and investigating synaptic function using techniques such as microelectrode arrays[32] is expected to provide

deeper insights. Nevertheless, our observation could be suggestive of a different effect on neuronal differentiation of the pathogenic *ARID1B* compared to the *SMARCB1* variants.

While some of the findings presented in this chapter can be considered preliminary, they already emphasize that the generation and implementation of different *in vitro* model systems, brings unique strengths to the study of the effects of CSS variants on neuronal development and function. Since many different cell types are present in the brain, it will be important to study the (dys)function in a developing patient's brain and more elaborate models that allow differentiation into multiple cell types (e.g. organoids) and/or more mature neurons are likely to shed more light on this. For instance, a recent study investigated agenesis of the corpus callosum, the most common brain anomaly in *ARID1B*[33], *SMARCB1*[17] and CSS patients[34,35]. Martins-Costa *et al*[12] showed, using neural organoids generated from an isogenic *ARID1B* patient line, disrupted axonogenesis. They identified a transcriptional dysregulation of callosal projection neurons, less long-range projections and, less contralateral synapses. These findings underline the hypothesis that interneuron disfunction plays an important role in the pathogenesis of CSS. The *in vitro* system we are employing can be used to investigate the differentiation from iPSC to GABAergic interneurons[27]. Therefore, building on the findings of Martins-Costa *et al*[12] and incorporating ATAC- and RNA-seq in our model system could further our understanding of the role of *ARID1B* and other CSS genes in interneuron development.

At the molecular level, the BAF complex primarily functions in regulating chromatin accessibility but DNA methylation alterations between control and CSS patients have been reported in blood. This so called episignature can be used in diagnostics[10] but it remains unclear whether it is also present in other cell types. Taking advantage of our *in vitro* model, we observe that the blood episignature is not present in patient derived iPSCs or NPCs (Figure 10b). Possible explanations could be that the BAFopathy pattern from blood is generated further in the differentiation process or that the observed episignature in blood is tissue specific.

The technology used to generate episignatures plays a significant role in the quality and consistency of results. The Illumina EPIC array versions 1[36] and 2[37], while widely used, are limited by batch effects and differences in probe coverage, with v1 covering 800,000 probe locations and v2 expanding to 900,000. We used the Illumina EPIC v2 array in our study, while the BAFopathy episignature was originally detected using the EPIC v1 array. However, we do not think this impacted our investigation of the BAFopathy episignature in iPSC and NPC, as 121 out of 131[10] episignature probes were reliably measured across all our samples. To overcome the limitations of the Illumina EPIC array, future research could leverage Nanopore sequencing[38]. This technology eliminates batch effects and

offers the ability to analyze over 28 million CpG sites[39], providing a more comprehensive overview of DNA methylation.

In sum, we successfully established an *in vitro* model system to explore the effects of genetic variants on neuronal differentiation, utilizing two *ARID1B*, three *SMARCB1* patient lines and four control lines. This model could be used for further investigation of the effects of pathogenic variants in CSS genes during differentiation and on the transcriptomic and epigenomic states.

REFERENCES

1. Vergano SA, van der Sluijs PJ, Santen G. ARID1B-Related Disorder. In: Adam MP, Ardinger HH, Pagon RA, et al, eds. *GeneReviews((R))*. 1993.
2. Santen GW, Aten E, Sun Y, et al. Mutations in SWI/SNF chromatin remodeling complex gene ARID1B cause Coffin-Siris syndrome. *Nat Genet*. Mar 18 2012;44(4):379-80. doi:10.1038/ng.2217
3. Tsurusaki Y, Okamoto N, Ohashi H, et al. Mutations affecting components of the SWI/SNF complex cause Coffin-Siris syndrome. *Nat Genet*. Mar 18 2012;44(4):376-8. doi:10.1038/ng.2219
4. Wieczorek D, Bogershausen N, Beleggia F, et al. A comprehensive molecular study on Coffin-Siris and Nicolaides-Baraitser syndromes identifies a broad molecular and clinical spectrum converging on altered chromatin remodeling. *Hum Mol Genet*. Dec 20 2013;22(25):5121-35. doi:10.1093/hmg/ddt366
5. Santen GW, Aten E, Vulto-van Silfhout AT, et al. Coffin-Siris syndrome and the BAF complex: genotype-phenotype study in 63 patients. *Hum Mutat*. Nov 2013;34(11):1519-28. doi:10.1002/humu.22394
6. Tsurusaki Y, Okamoto N, Ohashi H, et al. Coffin-Siris syndrome is a SWI/SNF complex disorder. *Clin Genet*. Jun 2014;85(6):548-54. doi:10.1111/cge.12225
7. Kosho T, Okamoto N, Ohashi H, et al. Clinical correlations of mutations affecting six components of the SWI/SNF complex: detailed description of 21 patients and a review of the literature. *Am J Med Genet A*. Jun 2013;161A(6):1221-37. doi:10.1002/ajmg.a.35933
8. Sekiguchi F, Tsurusaki Y, Okamoto N, et al. Genetic abnormalities in a large cohort of Coffin-Siris syndrome patients. *J Hum Genet*. Sep 17 2019;doi:10.1038/s10038-019-0667-4
9. Schrier Vergano S, Santen G, Wieczorek D, Wollnik B, Matsumoto N, Deardorff MA. Coffin-Siris Syndrome. In: Pagon RA, Adam MP, Ardinger HH, et al, eds. *GeneReviews(R)*. University of Washington; 1993.
10. Aref-Eshghi E, Bend EG, Hood RL, et al. BAFopathies' DNA methylation epi-signatures demonstrate diagnostic utility and functional continuum of Coffin-Siris and Nicolaides-Baraitser syndromes. *Nat Commun*. Nov 20 2018;9(1):4885. doi:10.1038/s41467-018-07193-y
11. Jung EM, Moffat JJ, Liu J, Dravid SM, Gurumurthy CB, Kim WY. Arid1b haploinsufficiency disrupts cortical interneuron development and mouse behavior. *Nat Neurosci*. Dec 2017;20(12):1694-1707. doi:10.1038/s41593-017-0013-0
12. Martins-Costa C, Wiegers A, Pham VA, et al. ARID1B controls transcriptional programs of axon projection in an organoid model of the human corpus callosum. *Cell Stem Cell*. May 6 2024;doi:10.1016/j.stem.2024.04.014
13. Pagliaroli L, Porazzi P, Curtis AT, et al. Inability to switch from ARID1A-BAF to ARID1B-BAF impairs exit from pluripotency and commitment towards neural crest formation in ARID1B-related neurodevelopmental disorders. *Nat Commun*. Nov 9 2021;12(1):6469. doi:10.1038/s41467-021-26810-x
14. Celen C, Chuang JC, Luo X, et al. Arid1b haploinsufficient mice reveal neuropsychiatric phenotypes and reversible causes of growth impairment. *Elife*. Jul 11 2017;6:e25730. doi:10.7554/eLife.25730
15. Shibutani M, Horii T, Shoji H, et al. Arid1b Haploinsufficiency Causes Abnormal Brain Gene Expression and Autism-Related Behaviors in Mice. *Int J Mol Sci*. Aug 30 2017;18(9)doi:10.3390/ijms18091872
16. Kim H, Kim D, Cho Y, et al. Early postnatal serotonin modulation prevents adult-stage deficits in Arid1b-deficient mice through synaptic transcriptional reprogramming. *Nat Commun*. Aug 27 2022;13(1):5051. doi:10.1038/s41467-022-32748-5

17. Filatova A, Rey LK, Lechler MB, et al. Mutations in SMARCB1 and in other Coffin-Siris syndrome genes lead to various brain midline defects. *Nat Commun*. Jul 4 2019;10(1):2966. doi:10.1038/s41467-019-10849-y
18. Ka M, Chopra DA, Dravid SM, Kim WY. Essential Roles for ARID1B in Dendritic Arborization and Spine Morphology of Developing Pyramidal Neurons. *J Neurosci*. Mar 02 2016;36(9):2723-42. doi:10.1523/JNEUROSCI.2321-15.2016
19. Smith AL, Jung EM, Jeon BT, Kim WY. Arid1b haploinsufficiency in parvalbumin- or somatostatin-expressing interneurons leads to distinct ASD-like and ID-like behavior. *Sci Rep*. May 12 2020;10(1):7834. doi:10.1038/s41598-020-64066-5
20. Valencia AM, Collings CK, Dao HT, et al. Recurrent SMARCB1 Mutations Reveal a Nucleosome Acidic Patch Interaction Site That Potentiates mSWI/SNF Complex Chromatin Remodeling. *Cell*. Nov 27 2019;179(6):1342-1356 e23. doi:10.1016/j.cell.2019.10.044
21. Kang E, Kang M, Ju Y, et al. Association between ARID2 and RAS-MAPK pathway in intellectual disability and short stature. *J Med Genet*. Nov 2021;58(11):767-777. doi:10.1136/jmedgenet-2020-107111
22. Li C, Fleck JS, Martins-Costa C, et al. Single-cell brain organoid screening identifies developmental defects in autism. *Nature*. Sep 2023;621(7978):373-380. doi:10.1038/s41586-023-06473-y
23. Crabtree G, Son E, Krokhotin A, Gourisankar S, Chang C-Y. ARID1B is a Dosage-sensitive Regulator of Polycomb Repressive Complex Distribution and HOX Gene Regulation in Patient-derived Neural Progenitors. Research Square; 2021.
24. Buijsen RAM, Gardiner SL, Bouma MJ, et al. Generation of 3 spinocerebellar ataxia type 1 (SCA1) patient-derived induced pluripotent stem cell lines LUMCi002-A, B, and C and 2 unaffected sibling control induced pluripotent stem cell lines LUMCi003-A and B. *Stem Cell Res*. May 2018;29:125-128. doi:10.1016/j.scr.2018.03.018
25. Chen J, Liu J, Chen Y, et al. Rational optimization of reprogramming culture conditions for the generation of induced pluripotent stem cells with ultra-high efficiency and fast kinetics. *Cell Res*. Jun 2011;21(6):884-94. doi:10.1038/cr.2011.51
26. Warlich E, Kuehle J, Cantz T, et al. Lentiviral vector design and imaging approaches to visualize the early stages of cellular reprogramming. *Mol Ther*. Apr 2011;19(4):782-9. doi:10.1038/mt.2010.314
27. Liu Y, Liu H, Sauvey C, Yao L, Zarnowska ED, Zhang SC. Directed differentiation of forebrain GABA interneurons from human pluripotent stem cells. *Nat Protoc*. Sep 2013;8(9):1670-9. doi:10.1038/nprot.2013.106
28. Sinke L, Cats D, Heijmans BT. Omixer: multivariate and reproducible sample randomization to proactively counter batch effects in omics studies. *Bioinformatics*. Sep 29 2021;37(18):3051-3052. doi:10.1093/bioinformatics/btab159
29. Moffat JJ, Jung EM, Ka M, Jeon BT, Lee H, Kim WY. Differential roles of ARID1B in excitatory and inhibitory neural progenitors in the developing cortex. *Sci Rep*. Feb 16 2021;11(1):3856. doi:10.1038/s41598-021-82974-y
30. Nagl NG, Jr., Wang X, Patsialou A, Van Scoy M, Moran E. Distinct mammalian SWI/SNF chromatin remodeling complexes with opposing roles in cell-cycle control. *EMBO J*. Feb 07 2007;26(3):752-63. doi:10.1038/sj.emboj.7601541
31. Raab JR, Resnick S, Magnuson T. Genome-Wide Transcriptional Regulation Mediated by Biochemically Distinct SWI/SNF Complexes. *PLoS Genet*. Dec 2015;11(12):e1005748. doi:10.1371/journal.pgen.1005748
32. Yuan X, Puvogel S, van Rhijn JR, et al. A human in vitro neuronal model for studying homeostatic plasticity at the network level. *Stem Cell Reports*. Nov 14 2023;18(11):2222-2239. doi:10.1016/j.stemcr.2023.09.011

33. van der Sluijs PJ, Jansen S, Vergano SA, et al. The ARID1B spectrum in 143 patients: from nonsyndromic intellectual disability to Coffin–Siris syndrome. *Genetics in Medicine*. 2018/10/22 2018;doi:10.1038/s41436-018-0330-z
34. van der Sluijs PJ, Joosten M, Alby C, et al. Discovering a new part of the phenotypic spectrum of Coffin-Siris syndrome in a fetal cohort. *Genet Med*. May 17 2022;doi:10.1016/j.gim.2022.04.010
35. Kosho T, Okamoto N, Coffin-Siris Syndrome International C. Genotype-phenotype correlation of Coffin-Siris syndrome caused by mutations in SMARCB1, SMARCA4, SMARCE1, and ARID1A. *Am J Med Genet C Semin Med Genet*. Sep 2014;166C(3):262-75. doi:10.1002/ajmg.c.31407
36. Pidsley R, Zotenko E, Peters TJ, et al. Critical evaluation of the Illumina MethylationEPIC BeadChip microarray for whole-genome DNA methylation profiling. *Genome Biol*. Oct 7 2016;17(1):208. doi:10.1186/s13059-016-1066-1
37. Peters TJ, Meyer B, Ryan L, et al. Characterisation and reproducibility of the HumanMethylationEPIC v2.0 BeadChip for DNA methylation profiling. *BMC Genomics*. Mar 6 2024;25(1):251. doi:10.1186/s12864-024-10027-5
38. Rand AC, Jain M, Eizenga JM, et al. Mapping DNA methylation with high-throughput nanopore sequencing. *Nat Methods*. Apr 2017;14(4):411-413. doi:10.1038/nmeth.4189
39. Silva C, Machado M, Ferrao J, Sebastiao Rodrigues A, Vieira L. Whole human genome 5'-mC methylation analysis using long read nanopore sequencing. *Epigenetics*. Dec 2022;17(13):1961-1975. doi:10.1080/15592294.2022.2097473

SUPPLEMENTARY TABLES AND FIGURES

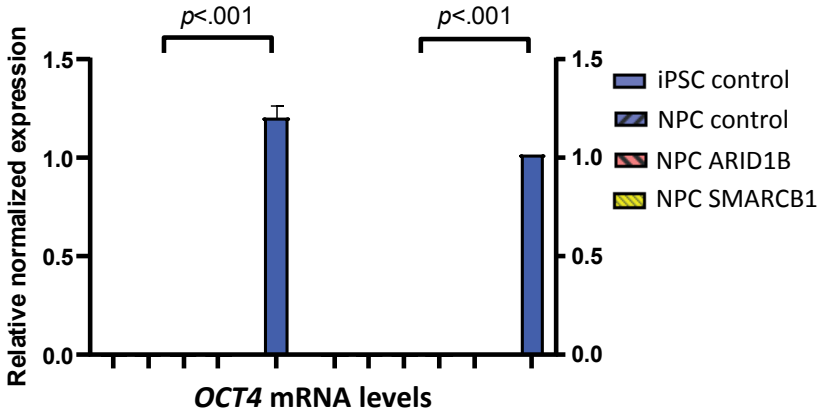

Supplementary Figure 1a: mRNA levels *OCT4* at differentiation day 12

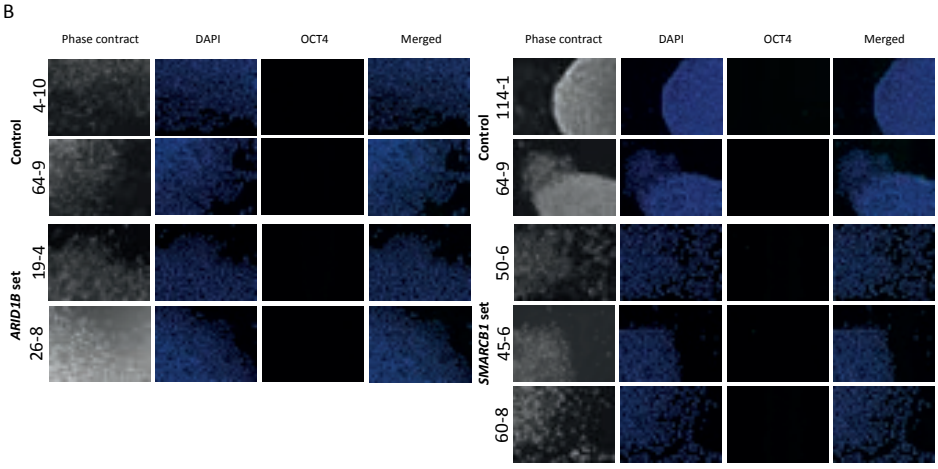

Supplementary Figure 1b: IF -staining of OCT4 on day 12 differentiated cells

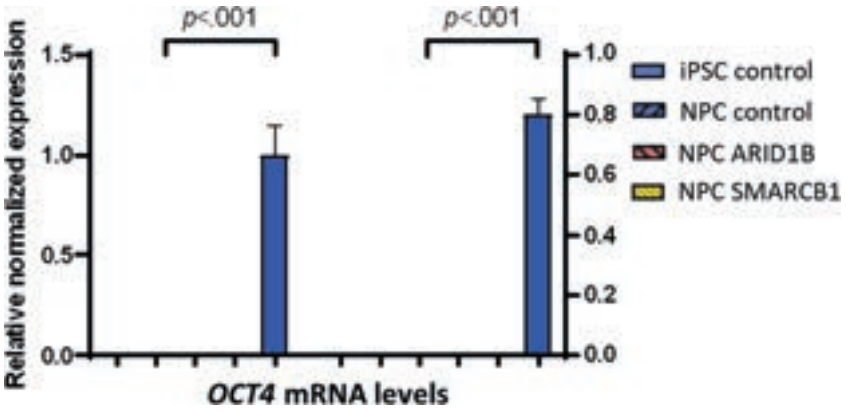

Supplementary Figure 2: mRNA expression of *OCT4* at differentiation day 16

Supplementary Table 1: Antibodies used for immunofluorescence

Antibody	Host	Article number	Dilution
OCT4	rabbit	ab19857	1:500
NANOG	rabbit	ab21624	1:500
SOX1	rabbit	Invitrogen PA5-23351	1:500
MAP2	mouse	MAB364, 3162484	1:500
Cleaved caspase-3	rabbit	rb9661S	1:500
anti-Rabbit 488	donkey	AlexaFluorTM 488 (A21206)	1:2000
anti-Mouse 594	donkey	AlexaFluorTM 594 (A21203)	1:2000
DAPI	-	R37605	

Supplementary Table 2: Primers used for RT-qPCR

	FW	**REV**	**Length**
Housekeeping gene			
GUS	CTCATTTGGAATTTTGCCGATT	CCGAGTGAAGATCCCCTTTTTA	81
Pluripotency markers			
OCT4	GACAGGGGGAGGGGAGGAGCTAGG	CTTCCCTCCAACCAGTTGCCCCAAAC	144
NANOG	AAGGTCCCGGTCAAGAAACA	TCTTCACCTGTTTGTAGCTGA	154
Neuronal (progenitor) marker			
NESTIN	CTCCAGAAACTCAAGCACC	TCCTGATTCTCCTCTTCCA	145
PAX6	GGTTGGTATCCGGGGACTT	TCCGTTGGAACTGATGGAGT	102
SOX2	AGCTCGCAGACCTACATGAA	TGGAGTGGGAGGAAGAGGTA	151
MAP2	AAGAGAATGGGATCAACGGAG	TGCTACAGCCTCAGCAGTGA	101
Genes			
ARID1B	GCGTGTGATGATGTCCCTTA	CCAGACAACTGGGAGAGATTG	123
SMARCB1	CTTCAGCGAGAACCCTCTGC	GCAAGACGCCTCATCCGC	156

Supplementary Table 3: median DNA methylation Beta values of individual samples

sample		median beta-value
iPSC	c1	0,697
iPSC	c2	0,772
iPSC	c3	0,753
iPSC	c4	0,712
iPSC	ARID1B_1	0,728
iPSC	ARID1B_2	0,709
iPSC	SMARCB1_1	0,748
iPSC	SMARCB1_2	0,746
iPSC	SMARCB1_3	0,788
Day 16	c1	0,801
Day 16	c2	0,722
Day 16	c3	0,775
Day 16	c4	0,761
Day 16	ARID1B_1	0,754
Day 16	ARID1B_2	0,717
Day 16	SMARCB1_1	0,779
Day 16	SMARCB1_2	0,758
Day 16	SMARCB1_3	0,761